UNIVERSITY of CALIFORNIA
SANTA CRUZ

VERITAS ANALYSIS OF SIX VERY HIGH ENERGY BLAZARS

A thesis submitted in partial satisfaction of the
requirements for the degree of

BACHELOR OF SCIENCE

in

ASTROPHYSICS

by

Brandon Cavins

10 June 2019

Abstract

VERITAS Analysis of Six Very High Energy Blazars

by

Brandon Cavins

In this paper data from the Very Energetic Radiation Imaging Telescope Array System (VERITAS) are analyzed using the VERITAS Gamma-ray Anaysis Suite (VEGAS). The results of the VEGAS analysis are shown for a total of six sources: Markarian 421 (Mrk 421), Markarian 501 (Mrk 501), PKS 1222+216, PKS 1441+25, 3C 279, and TON 599. TON 599 had a flare that lasted 2 days, MJD 58102 and MJD 58103. These days have a significance of 10.4σ, where σ is the standard deviation, while the rest of the data have a significance of 2.6σ. So, only the data from the flare are used in the analysis. A spectrum for TON 599 is created and it is deabsorbed using the Dominguez et al. 2011 model for the extra-galactic background light (EBL). The deabsorbed spectrum shows an expected trend line, which is a decrease in flux at higher energies, so the model is consistent with the data. The data from the VEGAS analysis for Mrk 421, Mrk 501, PKS 1222+216, PKS 1441+25, and 3C 279 were completed for a larger project called the line monitoring program. The line monitoring program is a project where the variability of gamma-ray observations is compared to the variability of optical spectral line fluxes. After running the VERITAS data through the VEGAS analysis, it was found that PKS1222+25 and 3C 279 do not have a high enough significance to register a detection. They have a significance of -0.3σ and 0.6σ respectively. Mrk 421 has a significance of 297σ, Mrk 501's significance is 59σ, and PKS 1441+25 has a significance of 5.9σ. Because these sources registered detections, their

flux values, obtained from the VEGAS analysis, are used to create light curves. While the correlation studies are incomplete, the VEGAS analysis, which is what this thesis presents, on these five sources is complete.

Contents

List of Figures

List of Tables

To Linda Morabito and David Meyer

Acknowledgments

I would like to thank my advisor, David Williams who has been patient with me and invaluable to my education. I would also like to thank the entire VERITAS team for allowing me to participate in their research. In addition to David Williams and the VERITAS team, thank you Terry Terhaar for the helpful feedback on this thesis. This work made use of data supplied by the UK Swift Science Data Centre at the University of Leicester.

1

Introduction

Active galactic nuclei (AGNs) are supermassive black holes that are powered by the accretion of matter onto the black hole. A blazar is an AGN whose relativistic jet is directed towards the Earth's line of sight. Many blazars emit gamma rays.

There are two categories that blazars fall under: flat spectrum radio quasars (FSRQs) and BL Lacertae (BL Lac) objects. FSRQs have stronger emission lines than BL Lacs in addition to being more luminous.

Blazars are characterized by their double-peaked spectral energy distribution (SED). An SED is a plot of energy versus frequency of light and can be used to show the emissions of different emission mechanisms. In the SEDs we obtain from blazars, the lower energy peak is attributed to synchrotron radiation and the higher energy peak can be produced by inverse-Compton upscattering.

Synchotron radiation is electromagnetic energy emitted by charged particles, such as electrons, moving at relativistic velocities when their path is altered, such as by a magnetic field. The charged particles move in a spiral along the direction of the magnetic field.

Compton scattering is the process in which a charged particle scatters a photon, resulting in a decrease in energy of the photon. Inverse-Compton upscattering is similar to Compton scattering, but the charged particle, the electron, has the higher energy and so the photon gains energy instead of losing it. There are two specific cases of Inverse-Compton upscattering that are thought to be occurring near the AGN: synchotron self-Compton (SSC) or external Compton (EC) scattering. SSC is the process in which the synchotron photons are upscattered by the electrons that created them. EC is the process where photons from an outside source, such as the jet, accretion disk, or the cosmic microwave background, undergo Comptonization by electrons .

A large fraction of the energy emitted from blazars is within the very high energy (VHE) band, making the study of VHE blazar spectra an essential part of understanding blazars. Researchers are currently studying these objects to determine whether VHE gamma-ray emissions are the result of leptonic or hadronic processes.

The extragalactic background light (EBL) is a diffuse light permeating the Universe as a result of star formation, active galactic nuclei (AGN), gas, and dust. The energy in the EBL is divided between light directly from stars, 52%, and light reemitted from dust, 48% (Hauser & Dwek, 2001). The EBL contains light from the past, making it an intriguing subject to study to determine qualities of the earlier Universe. However, it is difficult to observe the EBL directly, so, we use blazars as a probe to study the EBL. Some of the gamma-rays that blazars emit are absorbed by the EBL. This means that the gamma rays interact with the EBL to create electron-positron pairs, effectively removing the gamma-ray from our view. However, some of the gamma-rays make it to Earth unaffected by the EBL. Using the gamma-rays we detect, we can create a spectrum of the source. A spectrum is a plot of the flux as a function of energy. If we also apply our existing models for the EBL, we can create a deabsorbed spectrum of the blazar. To deabsorb a spectrum is to use our models of the EBL to determine what we would see if the gamma-rays were not affected by the EBL at all. If the deabsorbed spectrum is concave up, then our present model of the EBL has over-accounted for the absorbtion due to the EBL. If our model of the EBL is correct, the intrinsic blazar spectrum can be determined since the observed spectrum can be accurately deabsorbed.

The gamma-rays that make it to Earth interact with the atmosphere and create electron-positron pairs. This interaction causes a cascade of relativistic particles called an extensive air shower (EAS). These showers emit Cherenkov light, which is then detected by ground telescopes.

We use the Very Energetic Radiation Imaging Telescope Array System (VERITAS), an array of four gamma-ray telescopes located in southern Arizona, to detect Cherenkov radiation. Each telescope is 12 m in diameter and is comprised of mirrors that reflect Cherenkov photons onto a photomultiplier tube (PMT) detector package. Electronics are used to distinguish between background light and Cherenkov radiation (Holder et al, 2006).

1.1 Investigation of Optical Spectral Lines in Five VHE Blazars

The first project is the line monitoring program. The point of the line monitoring program is to compare the variability of gamma-ray observations to the variability of optical spectral line fluxes of five VHE gamma-ray emitters. Some of the spectral features are from the broad line region (BLR), but not all sources have a BLR. The BLR is the dense region where broad emission lines are formed. The five sources we are studying are: Markarian 421 (Mrk 421), Markarian 501 (Mrk 501), PKS 1222+216, PKS 1441+25, and 3C 279. These sources were chosen since they are bright in gamma-rays, variable, have been observed at least once per lunar month in 2016, and have absorption or emission lines in their optical spectra (Johnson, 2018). A lunar month is the time between two successive full moons. To determine the gamma-ray variability of these sources, light curves are created. Light curves are plots of the brightness as a function of time. This means that we can see how the brightness of a source changes over time. The outside of the jet dominates thermal emissions while the inside of the jet dominates non-thermal emissions. If the light curves of the thermal and non-thermal parts of the blazar show some correlation, then it is possible that the outside of the jet interacts with the inside. By comparing the variability in the spectral lines and the variability in gamma-ray brightness, we hope to learn more about how and where gamma rays are produced in the blazar. The line monitoring program is a collaboration among many people, but the portion presented here is to run the VERITAS Gamma-ray Anaysis Suite (VEGAS) on each of the sources. This part of the project is complete, but we are currently waiting for other components of the project to be complete before we can continue.

1.2 Study of the FSRQ TON 599 and its Spectrum

TON 599 is another blazar that was first observed by VERITAS in 2017 (Mukherjee, 2017). Using data gathered from VERITAS, we are studying TON 599's VHE spectrum. TON 599 is the second most distant source that VERITAS has detected and the third most distant that any VHE telescope has detected, with a redshift of z = 0.725 (Hewett & Wild, 2010; Schneider et al, 2010). Because TON 599 is a distant source, it is more heavily affected by the EBL than sources that are closer. This is because its gamma rays travel more through the EBL than a closer source's gamma-rays. This makes TON 599 a good candidate to study to gain insight into past conditions of the Universe.

This paper presents the process of detecting Cherenkov radiation, the analysis software that was used, and what we found by studying the five sources in the line monitoring program and TON 599.

2

Methods

2.1 Detecting Cherenkov Radiation

The calibration of the telescopes is done by using a flasher system to test each PMTs nominal operating region. The flasher system is an assembly of seven blue LEDs, that can be turned on and off to vary the brightness, that shine flashes of light through a diffuser that then spreads the light to the PMTs (Hanna et al, 2009). Calibrating in this way reveals the relative gains and timing offsets of the pixels. Flasher runs are taken at some time during the night of the observations, however, it is rarely done at the beginning of the night. Each telescope is assigned a flasher run for analysis of the data.

Data are gathered by pointing the telescope array at the source for a span of thirty minutes. However, observations are not always taken for thirty minutes. For example, if the weather becomes bad in the middle of the observation, then the observers may decide that it is not beneficial to continue observing that source. Every observation of a source is called a run and each run is assigned a run number to identify it.

Each PMT sends signals to both the constant fraction discriminator (CFD) and the flash analog-to-digital converter (FADC). The FADC's task is to take the output voltage from the PMT and convert it to digital counts. The CFD determines whether a signal from a PMT is bright enough to count as a detection. There are three observing modes that determine what the threshold for the CFD is set to. The first is dark time observing. This is the ideal case where the moon is either below the horizon or if it is not bright enough to cause PMT currents greater than 10 μA. The CFD threshold is set to 45 mV in this case. The second observing mode is moonlight observations, which is when current in the PMTs caused by moonlight is in the range of 10 μA to 15 μA. For moonlight observations, the CFD's threshold is raised to 65 mV. The final observing mode is the reduced high voltage (RHV) mode. PMTs degrade with extensive exposure to light, so when the moon is particularly bright, the high voltage supplied to the PMTs is reduced to 81% of its normal value. When observing in the RHV mode, the CFDs threshold is reduced to 25 mV. If, while using the RHV mode, PMT currents exceed 10 μA, then observations are not taken. The observation mode is chosen by the observers.

VERITAS has a 3-level trigger system to determine if an actual event is observed, or if it is just a fluctuation in the background. The 3 levels in the trigger system are: L1, L2, and L3. The L1 trigger is the CFD. It checks the individual pixels and determines if a signal reaches the CFD's threshold. The next trigger level, L2, determines if an individual telescope registers a detection. This is done by checking if 3 neighboring pixels pass the L1 trigger, within 5-10 ns of each other. The L2 trigger helps remove L1 triggers caused by fluctuations in the background. The L3 trigger level operates on the array as a whole. The L3 trigger determines if more than one telescope was triggered in a span of 50 ns. Time delays from the differences in travel time for the Cherenkov showers are taken into account. The L3 trigger is good for removing noise caused by muons because they are typically only seen in one telescope. Once the L3 trigger is passed, the data are read out. However, whenever data are read out, observing time is lost, this is called deadtime. The 3-level trigger system diminishes the deadtime by only reading out signals that pass all 3 levels.

Each run has a number of plots associated with it, created after the run is complete. They are used to determine the quality of the data for that run. These plots are saved to a system called the Data Quality Monitoring image viewer, abbreviated as DQM. Some of the DQM plots include a plot of the far infrared (FIR) temperature, the L3 rate, and the L3 time cut. Examples of these plots are shown for run number 88396, which is in Table F1. This run was chosen since most of its plots are clear to understand.

The FIR sky temperature versus time plot indicates the weather conditions throughout the duration of the run. This is because the FIR temperature will increase when there are clouds due to the fact that a cloud has a higher temperature than a clear sky. If the FIR plot indicates that the weather for that run was bad, then we do not use that run in our analysis. If, however, there are only certain times that show bad weather, then those times are cut from the analysis. When times are cut from the analysis, it is called a time cut. Figure 2.1 shows the FIR plot for run number 88396. This particular FIR plot shows good weather since there is not a lot of variability in the FIR temperature.

The L3 rate plot is a plot that shows the trigger rate of detections as a function of time. The trigger rate is the rate at which the telescopes register a detection and it is measured in hertz. This plot should be stable throughout the run; high variability is an indication of bad weather since the clouds will diminish the trigger rate. However, it is

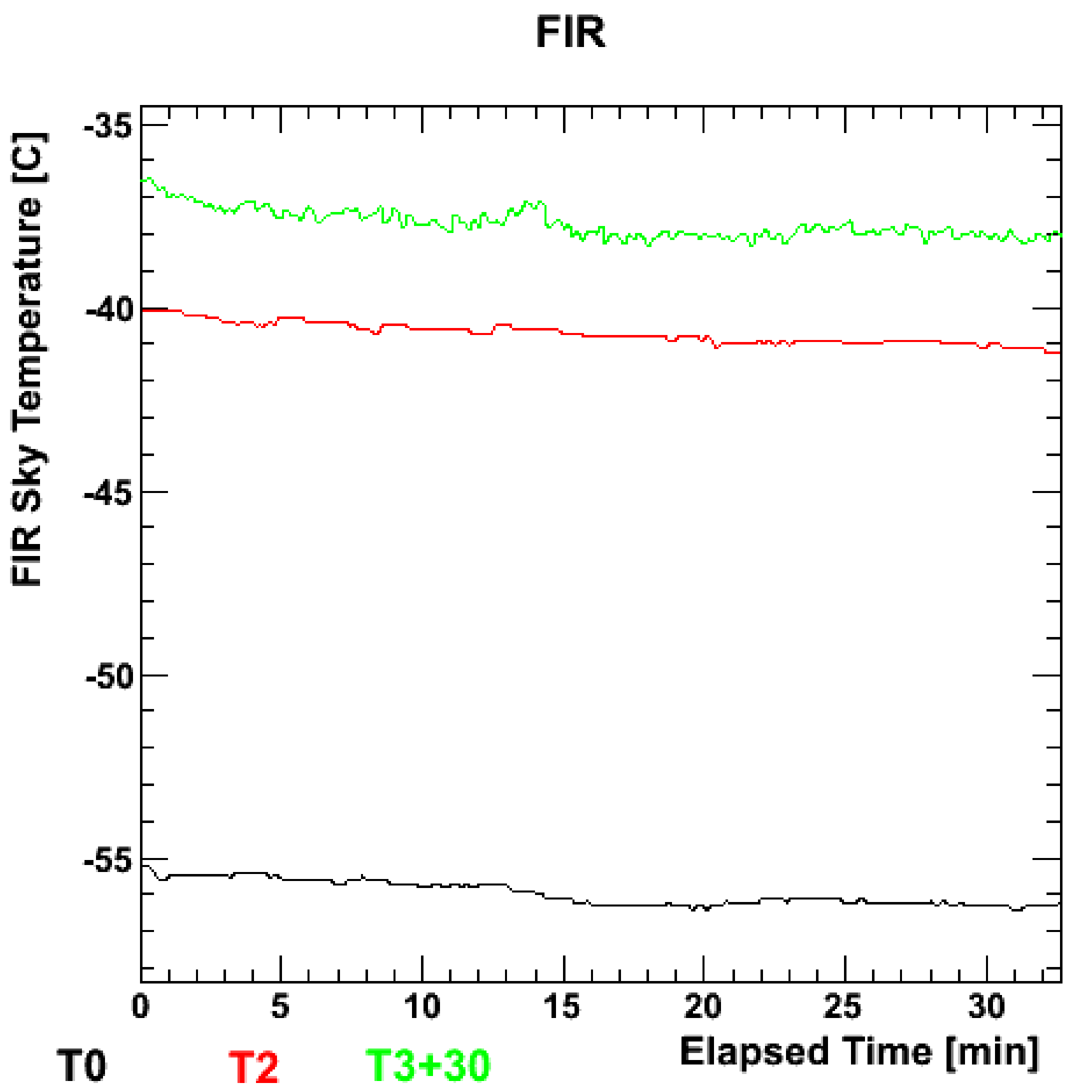

Figure 2.1: The DQM plot of the FIR temperature for run number 88396. T0 is mounted in a fixed position and has a wider field of view. T2 and T3+30 are mounted on telescopes, so they point where the telescopes are pointed. They have more narrow field of views. The "+30" in T3+30 signifies that 30° is added to the T3 value.

normal for trigger rates to drop at lower elevations since there is more atmosphere to go through, the Cherenkov light will be created further from the telescope array. This means less Cherenkov light is detected at lower elevations. An example of this plot is shown in Figure 2.2. The L3 time cut plot is similar to the L3 rate plot. The difference is that the L3 time cut plot is designed to identify times in the run that need to be cut out so that we don't analyze any inaccurate data. A time cut is automatically applied when the L3 rate varies by more than 10% from the baseline, which is the median of the L3 rate. This plot is checked manually to determine if the time cuts are warranted and if they are not, they are removed. In addition, new time cuts are added when necessary. Figure 2.3 shows an example of this plot. The blue area of the plot shows the time cut for run 88396, which is from 0 seconds to 180 seconds.

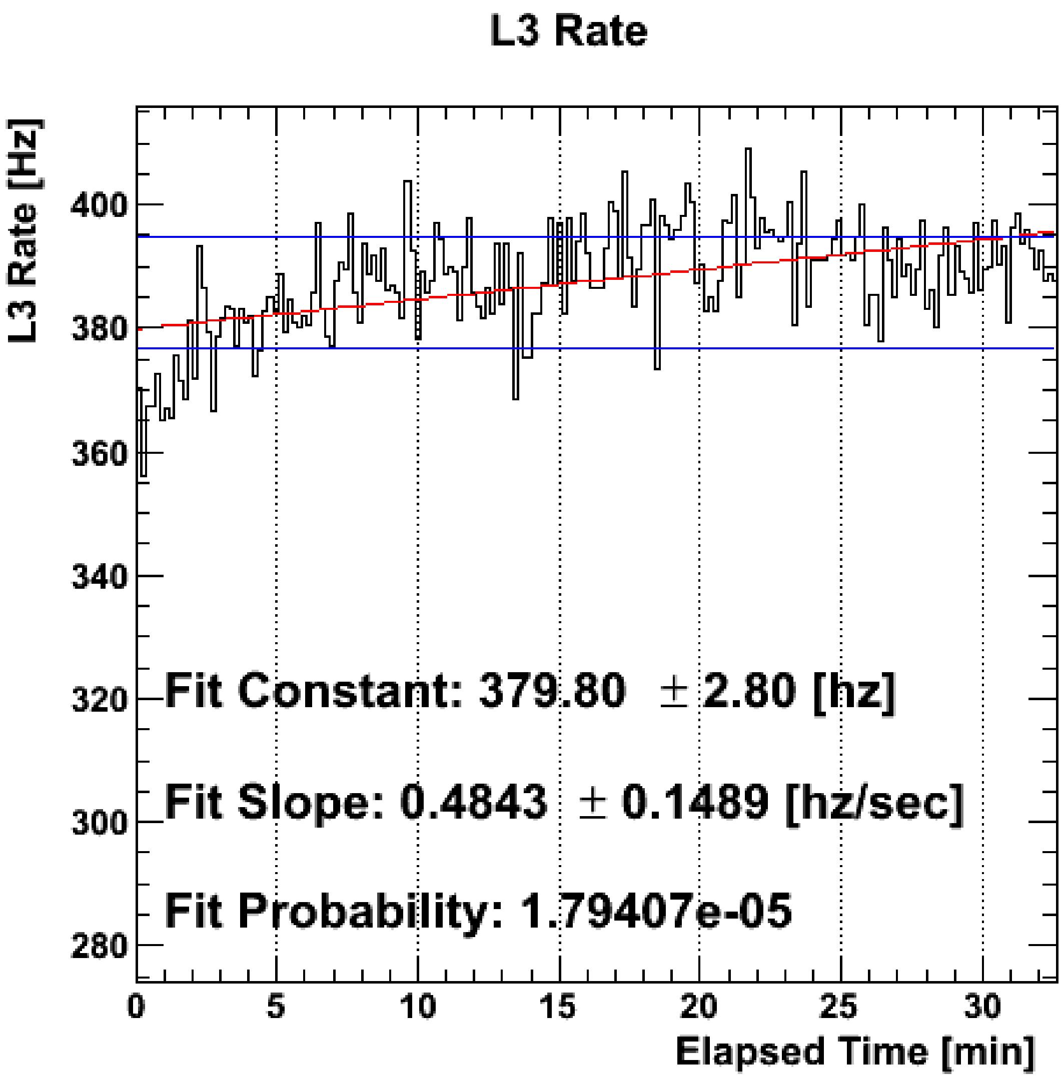

Figure 2.2: The DQM plot of the L3 rate for run number 88396.

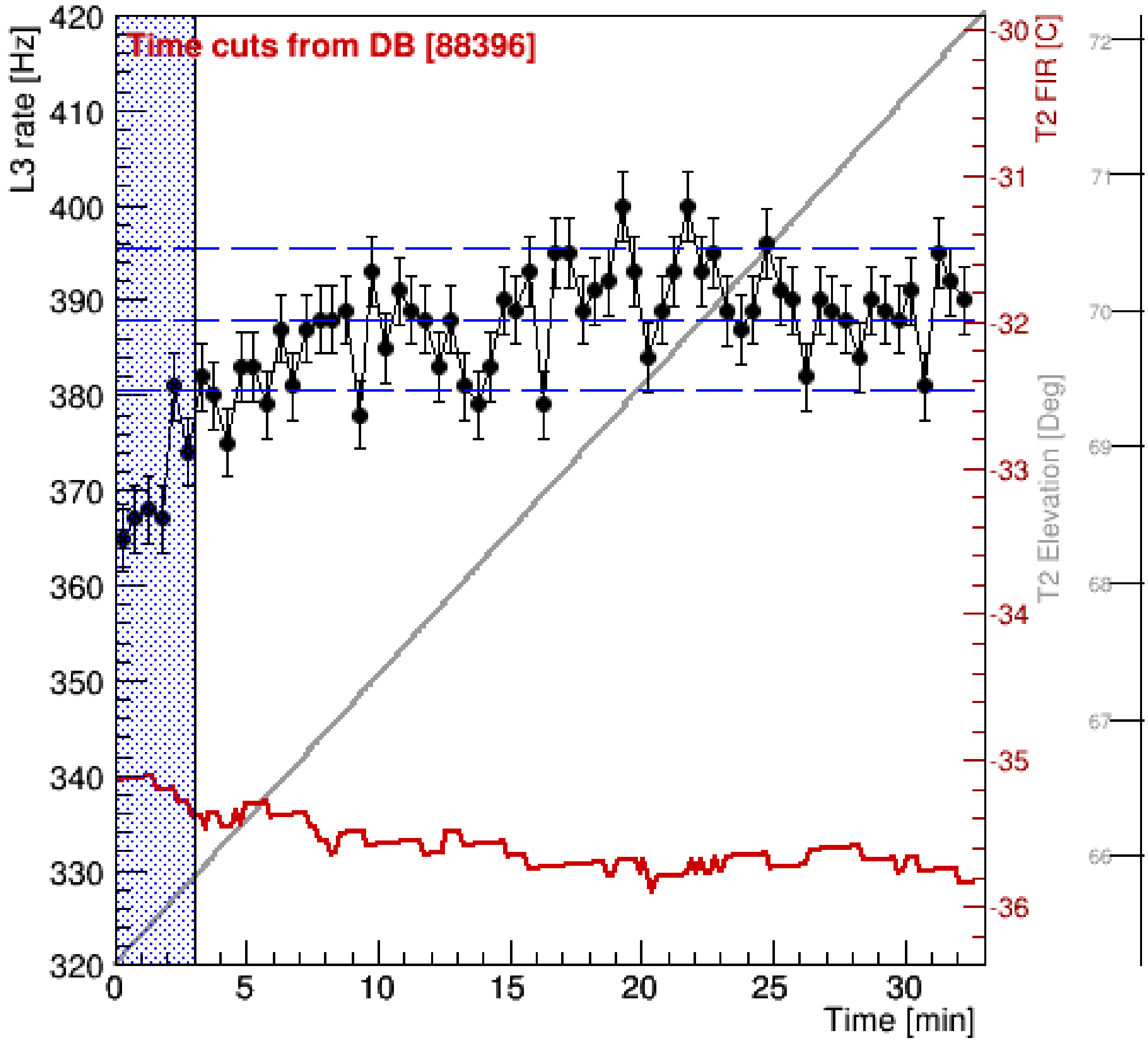

Figure 2.3: The DQM plot of the L3 time cut for run number 88396.

Using these plots, in addition to many other plots included in the DQM, we determine if the run is acceptable and if so, if we need to apply time cuts. Once we have this information, we then add the run number and any time cuts to a text file. This file is called a runlist.

2.2 VEGAS Analysis

The VERITAS Gamma-ray Anaysis Suite (VEGAS) is a data-analysis software package created by the Offline Analysis Working Group (OAWG), a subset of the VERITAS collaboration. The purpose of VEGAS is to process data from the telescope array so that we can analyze it. VEGAS has 5 stages: stage 1, stage 2, stage 4, stage 5, and stage 6. Stage 3 is deprecated and is no longer included in the VEGAS analysis. Stage 1 reads the raw telescope data into the software. It then calculates hardware-specific calibration and collects information on the array. Stage 2 takes the calibration data from stage 1 and applies the calibration constants to the data. Each event is looked at individually. Every event creates an image from each telescope, which is parameterized individually as an ellipse. The image size is the total charge in all of the pixels in the image. Stage 4 reconstructs the Cherenkov showers by combining the images obtained from stage 2. It also reconstructs specific properties of the shower such as its direction and energy of the individual events. Quality cuts are applied to each image in this stage. The quality cuts are determined by using the image distance, which is the distance between the ellipse centroid and the center of the camera, the image size, and the number of pixels. There are 3 sets of cuts that have been optimized based on past observations. The 3 sets of cuts are: soft, medium, and hard. Hard spectra have a more shallow slope, while soft spectra have steeper slopes. So, if a shallow slope is expected, then hard cuts are used, if a medium slope is expected, then medium cuts are used, and if a steep slope is expected, then soft cuts are used. If after creating the spectrum, it is realized that a different set of cuts would have been better, then the VEGAS analysis is re-run using the appropriate set of cuts. Table 2.1 shows the requirements that need to be set in stage 4 based on the cuts used. Stage

Cuts	Size Lower
Soft	400
Medium	700
Hard	1200

Table 2.1: The parameters for stage 4 of VEGAS based on what cuts are used. The Size Lower is the minimum number of digital counts required for an image for each set of cuts.

Cuts	MSL	MSW	Max Height Lower
Soft	$0.05 < \text{MSL} < 1.3$	$0.05 < \text{MSW} < 1.1$	7 km
Medium	$0.05 < \text{MSL} < 1.3$	$0.05 < \text{MSW} < 1.1$	7 km
Hard	$0.05 < \text{MSL} < 1.4$	$0.05 < \text{MSW} < 1.1$	None

Table 2.2: The parameters for stage 5 of VEGAS based on what cuts are used. The mean scaled length (MSL) and mean scaled width (MSW) refer to the image dimensions. They are used to distinguish extensive air showers created by gamma-rays and those created by cosmic rays. The max height lower refers to the lower limit of the shower maximum, which is the height in the atmosphere where the most Cherenkov light is emitted and where the most particles are created in the extensive air shower. Table adapted from Johnson (2018).

5 separates each event into three categories: gamma-ray-like, hadron-like, or potentially corrupted. The events are categorized based on their reconstructed properties. Table 2.2 shows the ranges that the properties need to be in for the event to be classified as a gamma-ray event based on the cuts used. Stage 6 is where the scientific results are calculated. In this stage, the gamma-ray-like events are combined from all of the runs and are put through a final statistical analysis. The parameters for each set of cuts is shown in Table 2.3. Stage 6 has three major output products: the sky map, a light curve, and a spectrum.

There are two methods used for the reconstruction of gamma-rays in VEGAS:

Cuts	S6A Ring Size	RBM Search Window Square Cut
Soft	0.17	0.03
Medium	0.1	0.01
Hard	0.1	0.01

Table 2.3: The parameters for stage 6 of VEGAS based on what cuts are used. The S6A Ring Size defines the angular size of the region used in the analysis. The RBM search window square cut is the squared angular radius of the on-source searching window.

standard hillas method (STD) and the image template method (ITM). The standard method uses weighted averages of information from the air-shower images to reconstruct the gamma-ray direction. The image template method uses templates to predict the number of counts in each pixel of the camera. The templates are produced from Monte Carlo simulations of gamma-ray showers. The templates are adjusted based on the gamma-ray energy and incident direction to find the best match to the counts in each pixel. A drawback of using the standard method is that the analysis is affected by missing information. Examples of missing information are a removed pixel due to bright starlight or images that are beyond the edge of the camera. The image template method does not average over the information from the images like the standard method does. This makes the image template method less susceptible to missing information. The main difference between the standard method and the image template method is that the theta squared cut is smaller for the image template method. The exact direction of where the gamma ray comes from is unknown, so a theta squared cut is used to create a circular region in the sky for VERITAS to observe. For each gamma ray, the analysis predicts the direction it came from. Then, the predicted direction is compared to the actual direction of the source. The difference between these two angles is theta. If theta is large, then the angle between the predicted direction and true direction is large. This means that the event is likely not to be from the source. A small theta implies the opposite, so it is likely that the gamma ray was from the source. However, it could be background. If the detector and the event reconstruction were perfect, then the distribution of theta would be a delta function centered at 0. This would mean that the theta squared cut could be made arbitrarily small. Since the image template method does a better job of reconstructing the gamma-ray directions than the standard method, then the typical values of theta for genuine signal events will be smaller for the image template method than the standard method, allowing the user to make a smaller theta, and thus theta squared, cut. The image template method helps reveal more about the EBL due to its more accurate statistics.

2.2.1 VIVA

The Very Independent VEGAS Analysis (VIVA) is a pipeline that we use to interface with the VEGAS analysis. VIVA allows us to define runlists we want to use and parameters for each stage of VEGAS. To use VIVA we first create an instructions file, which is a file that tells VIVA which stages to run and what parameters to set for each stage. The instructions file also includes paths to each runlist that is being used. One of the parameters that needs to be set is the atmosphere. The atmosphere refers to the time of the year that the observations were taken. There are two different atmospheres that VEGAS uses, ATM21 and ATM22. ATM21 is the winter atmosphere and it includes all observations taken between November and April. ATM22 is the summer atmosphere and it includes observations taken between May and October. However, the exact days that each atmosphere starts and ends on vary.

The atmosphere that the observations were taken in change the effective area of the telescope array. The peak effective area of the array is 100,000m^2, this is related, but not equal, to the physical area of the array. Because Cherenkov light spreads out from the axis of the air shower, the shower itself does not necessarily need to land within the array's area to be detected. A brighter, more energetic shower can land farther away and still be detected than a less bright, less energetic shower. How the showers develop is varied, especially how deep into the atmosphere they develop. The depth at which the shower develops affects the amount of light that reaches the ground, thus affecting the probability of detecting the shower. The probability of detecting a shower is in the range of 0 to 1 and is dependent on the energy and position. The overall rate of detected events given a flux of gamma rays on the array can be calculated by scattering gamma rays around the telescopes at random positions and seeing what fraction are detected. If a perfect detector were used that could detect all of the gamma rays within some area, and did not detect any that is outside of that area, then the size of an idealized detector that gives the same rate of detected events as the real detector is the effective area. The effective area is dependent on the number of operational telescopes, energy, and the set of cuts that is used. The effective area is calculated using Monte Carlo simulations. Monte Carlo simulation creates models of possible results by substituting a probability distribution for any factor that is inherently uncertain. The simulation recalculates the results with different values until it is complete. There are pre-made effective area files that were created through Monte Carlo simulation. We pass the appropriate effective area to VIVA in stage 6, depending on the atmosphere, the cuts used, the analysis method, and which telescopes were operational at the time of observation.

In addition to the pre-made effective area files, we also have pre-made lookup tables. A lookup table is an array that contains data that would otherwise need to be calculated at runtime, which would increase the computation time. The lookup tables we use contain information on the energy of a gamma-ray as a function of the background noise level, the size, impact distance, and the direction the telescopes are pointing. They also contain the average width and length for gamma ray images.

To create a spectrum, some parameters need to be set in stage 6. The spectral index is a measure of the dependence of the flux density as a function of frequency. The spectral index is related to the hardness, which is the steepness, of the spectrum. To determine the spectral index needed for a given source, the spectral index that is passed to stage 6 is iterated. Iterating the spectral index is necessary because the effective areas rely on the spectrum. However, the spectrum is dependent on the effective area used. So, if the spectrum has a different spectral index than was put in, then the effective area needs to be adjusted by creating a new spectrum with the new spectral index. This process is repeated until the analysis returns the same spectral index that is passed in. The spectrum is created through a binning method. This binning method has to do with the calculation of the flux. To calculate the flux, we need the number of excess counts, the live time, and the effective area binned in terms of energy. The number of excess counts is the number of counts observed minus the background, so, a significant amount of excess counts indicates a detection. The binning of the energy is important because statistical analysis is run on each bin and a significance for each bin is returned. The significance is a measure of how certain we are that there was actually a detection as opposed to random fluctuations. In order for a bin to be used to construct the spectrum, it must have a significance of at least 2σ, where σ is the standard deviation, and an excess counts of at least 5.

2.3 Analysis of the 5 Blazars in the Line Monitoring Program

The analysis of these sources was done using the standard method. We use the standard method since the image template method didn't become an accepted method until after the line monitoring program was started.

The runlists referred to in this chapter are shown in the appendix. The format is such that each run number is on its own line and if there are any timecuts, they are shown by the numbers after the run number. For example, for Table A1, the fourth line down shows run number 80642 with three time cuts from 840 to 960 seconds, 1000 to 1200 seconds, and 1380 to 1500 seconds. The seconds refer to the amount of time elapsed since starting the observation. Separate runlists are created for observations that were taken while one of the telescopes was not operating and for the different atmospheres.

2.3.1 Markarian 421

Mrk 421 is a BL Lac and has a redshift of z=0.031. The runlists in Appendix A show the runlists we use for Mrk 421. We use medium cuts for Mrk 421, which means we use the effective area files that correspond to medium cuts and the standard analysis method. However, the specific effective area is different for each runlist because they are either in a different atmosphere or they have different operational telescopes. Mrk 421's data were analyzed from observations taken between 15 December 2015 and 29 April 2018. It has a live time of 48.49 hours, which is the total time that the source was observed.

2.3.2 Markarian 501

Mrk 501 is a BL Lac and has a redshift of z=0.034. The runlists we use for Mrk 501 are shown in Appendix B. Like Mrk 421, Mrk 501 uses medium cuts. Analysis was done on observations between 22 February 2016 and 27 June 2018, leading to a live time 23.88 hours.

2.3.3 PKS 1222+216

PKS 1222+216 is an FSRQ and has a redshift of z=0.432. PKS 1222+216 has its runlists stored in Appendix C. PKS 1222+216 uses soft cuts and thus the effective area file and lookup tables reflect that. PKS 1222+216 had its data analyzed from 25 December 2015 to 8 June 2017. The live time is 3.40 hours.

2.3.4 PKS 1441+25

PKS 1441+25 is an FSRQ and has a redshift of z=0.940. The runlists for PKS 1441+25 are shown in Appendix D. PKS 1441+25 also uses soft cuts. The analysis takes into account observations taken from 4 April 2015 to 27 June 2018. This results in a live time of 25.56 hours.

2.3.5 3C 279

3C 279 is an FSRQ and has a redshift of z=0.5362. 3C 279's runlists are held in Appendix E. 3C 279 uses soft cuts as well. Observations that were analyzed ranged from 24 January 2016 to 27 June 2018. The live time for this period is 11.83 hours.

2.3.6 Optical Spectra

The optical spectra for each source were taken at the Lick Observatory with the exception of one spectrum taken at the Keck observatory. The Lick Observatory uses the Kast Double Spectrograph to get the spectra. The Kast instrument consists two separate spectrographs, one optimized for red wavelenghts and the other for blue. They, however, do share some components. Beamsplitters and charge-coupled devices (CCDs) allow for both the red and blue spectrographs to observe at the same time.

2.3.7 Creating the Light Curves

Each source is run through VEGAS, and then they are separated into lunar months, as explained in the Introduction. To do this, runlists are created for each lunar month. Once the runs are separated, we then run only stage 6 on each of these runlists. By doing this, we are able to get flux calculations, which is the desired value we need to create light curves.

2.4 Analysis of TON 599

For TON 599, we use the image template method since it provides better results than the standard method. This method has been tested on other sources and has been proven to provide a higher signal to noise ratio. The image template method is used for TON 599 but not for the line monitoring program because the image template method was not an accepted method when the line monitoring program was started. TON 599 uses soft cuts and its runlists are listed in Appendix F. The deabsorption of TON 599's spectrum is done using the Dominguez et al. (2011) model of the EBL.

After noticing that there were two days where TON 599 had a flare, we decided to isolate these two days. The two days in question are MJD 58102 (December 15, 2017) and MJD 58103(December 16, 2017). MJD stands for modified Julian date and it is another way to specify a date. We first ran VEGAS on just these two days, then we ran VEGAS on all of the data, except the two days. The reason for this is so that we can determine the significance of the flare versus the significance of the rest of the data. In addition to isolating the two days, we analyzed each day by itself to determine if the flare only took place on one of the days and not both.

In addition to analyzing the VERITAS data, we also analyzed Swift X-ray Telescope (XRT) data. The XRT is an instrument on the Neil Gehrels Swift Observatory satellite that was designed to measures fluxes, light curves, and spectra from gamma-ray bursts (Gehrels et al, 2004). However, it is also used to observe other sources as well, such as TON 599. The data are analyzed on Swift's data analysis website (Evans et al, 2007; Evans et al, 2009). We analyzed the two days separately from the rest of the data and isolated each day as we did with the VERITAS data.

3

Results

3.1 Line Monitoring

After running an analysis on each of the five sources, we found that three of them had a significance large enough to declare, with a high degree of confidence, a detection of the source. These three sources are Mrk 421, Mrk 501, and PKS 1441+25.

3.1.1 Sources With No Detection

PKS 1222+216 has a significance of -0.3σ and 3C 279 has a significance of 0.6 σ. These significance values indicate that during our observations of these sources we did not register a detection. As a result, we are unable to carry out correlation studies on these sources.

3.1.2 Sources With Detection

Mrk 421 has a significance of 297σ and Mrk 501 has a significance of 59σ. PKS 1441+25 has a significance of 5.9σ. These significance values indicate that we did register a detection for these sources, however, correlation studies were not carried out for Mrk 421 and Mrk 501 because they do not show definitive emission or absorption lines associated with the thermal components of their emissions (Johnson, 2018). PKS 1441+25 shows strong absorption and emission lines, but its flux values for the Kast spectra are inaccurate due to bad weather. These studies are incomplete, however, since we are waiting for collaborators to complete their parts of the project.

3.1.3 VERITAS Light Curves

Figures 3.1, 3.2, and 3.3 show the light curves for Mrk 421, Mrk 501, and PKS 1441+25 respectively. These light curves were created using the VERITAS data from this analysis, but, they were created by Johnson (2018). Mrk 421 and Mrk 501 show high variability, which is why they were chosen for this study. PKS 1441+25 has large error bars due to the fact that bad weather causes large time cuts. This means that the amount of data that can be analyzed is diminished, making it difficult to determine the variability of PKS 1441+25. The gray, dashed lines show the dates that spectra were taken from the Kast instrument at Lick observatory.

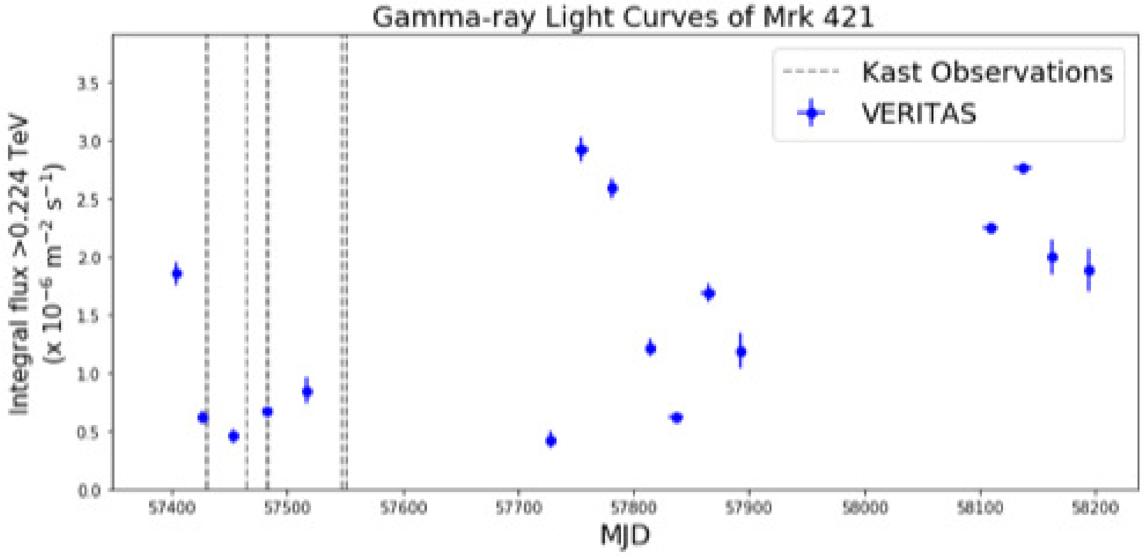

Figure 3.1: The VERITAS light curve for Markarian 421. The points show the flux value for the given lunar month and the vertical lines show the uncertainty in the measured value. The gray dashed lines show the dates that the Kast spectra were taken. (Johnson, 2018)

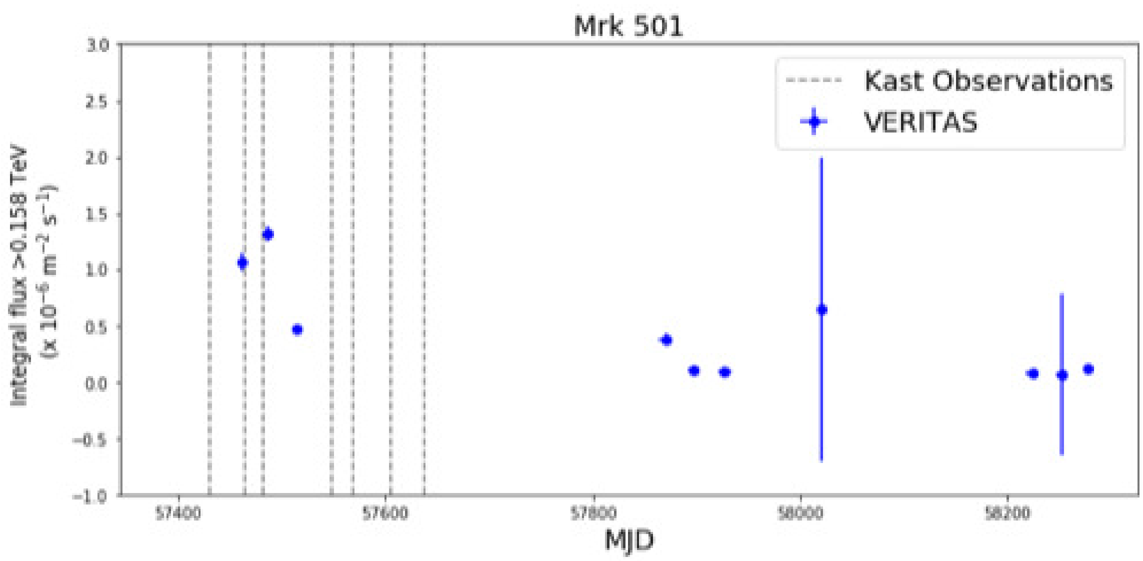

Figure 3.2: The VERITAS light curve for Markarian 501. The points show the flux value for the given lunar month and the vertical lines show the uncertainty in the measured value. The gray dashed lines show the dates that the Kast spectra were taken. (Johnson, 2018)

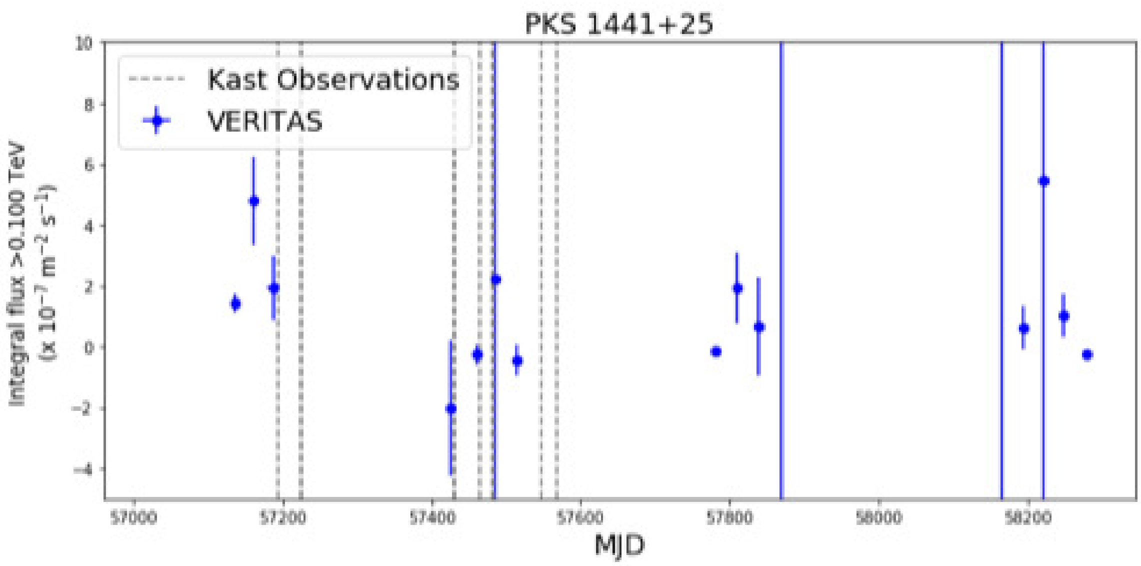

Figure 3.3: The VERITAS light curve for PKS 1441+25. The points show the flux value for the given lunar month and the vertical lines show the uncertainty in the measured value. Some of the points are off of the figure with large error bars, which is why there are blue vertical lines with no points associated with them. The gray dashed lines show the dates that the Kast spectra were taken.(Johnson, 2018)

3.1.4 Kast Spectrum

Figure 3.4 shows an example of a Kast spectrum for 3C 279. This is just one example of a Kast spectrum, more spectra were created for 3C279 as well as for the other four sources. Their analysis was not part of the work for this thesis.

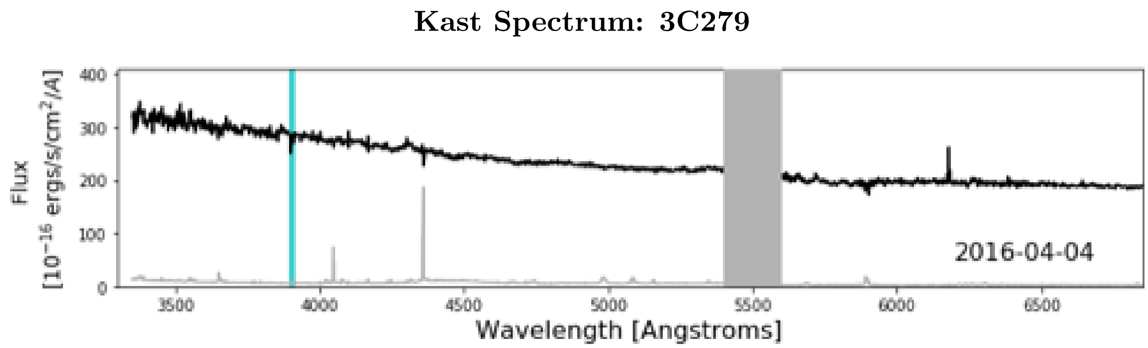

Figure 3.4: An example of a Kast spectrum for 3C 279. The black line is the flux, the grey line below that is the uncertainty of the flux, the blue line shows the MgII absorption feature, and the large grey rectangle shows an instrumental gap. (Johnson, 2018)

3.2 TON 599

After isolating the flare that lasted two days, we found that the flare had a significance of 10.4σ, which means we registered a detection for these two days. However, the rest of the data only had a significance of 2.6σ. This is not significant enough to register a detection. After isolating each day, we determined that the flare was active for both days as shown by Figure 3.5. This figure shows that both days have similar fluxes as a function of energy. The VEGAS analysis shows that detections were made for each day with significances of 6.2σ and 8.5σ.

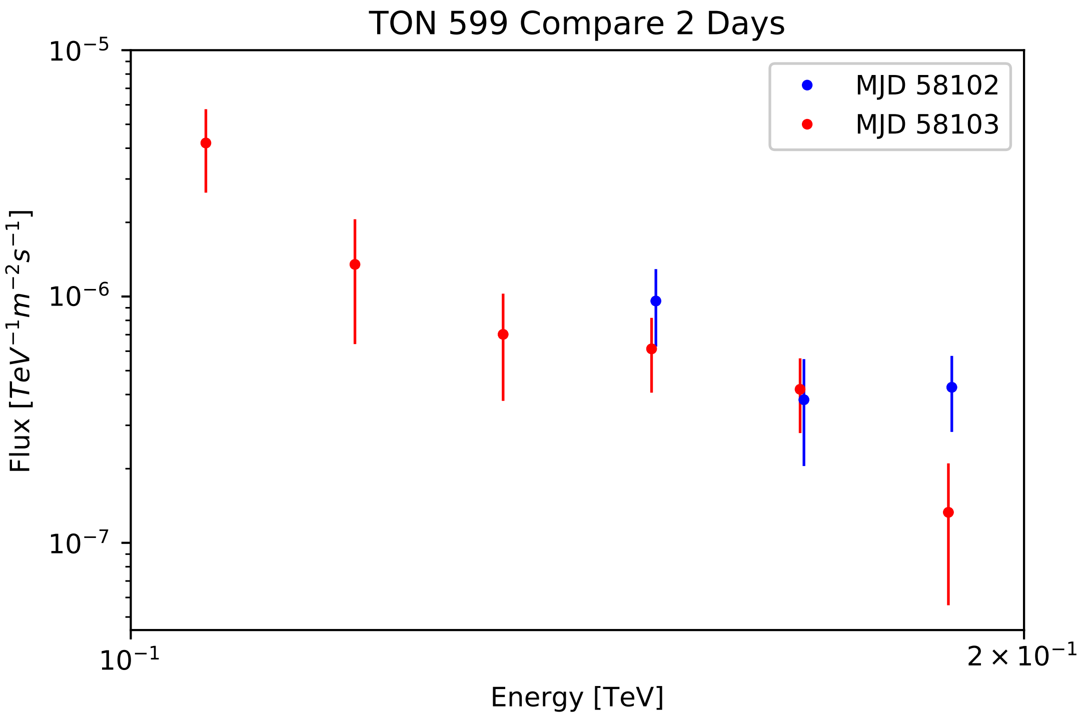

Figure 3.5: Each day of the flare plotted separately. The data taken on MJD 58102 are shown in blue and the data taken on MJD 58103 are shown in red.

3.2.1 Swift-XRT Light Curve

The claim that the 2 days have similar fluxes is further supported by Figure 3.6, which shows the Swift-XRT light curve for MJD 58102 and MJD 58103. Neither one of the days has a substantially larger count rate than the other, which indicates that the flare occurred over the course of both days. Since there is only a detection for the two days and each day has a similar flux, we analyzed the two days together and did not use the rest of the data.

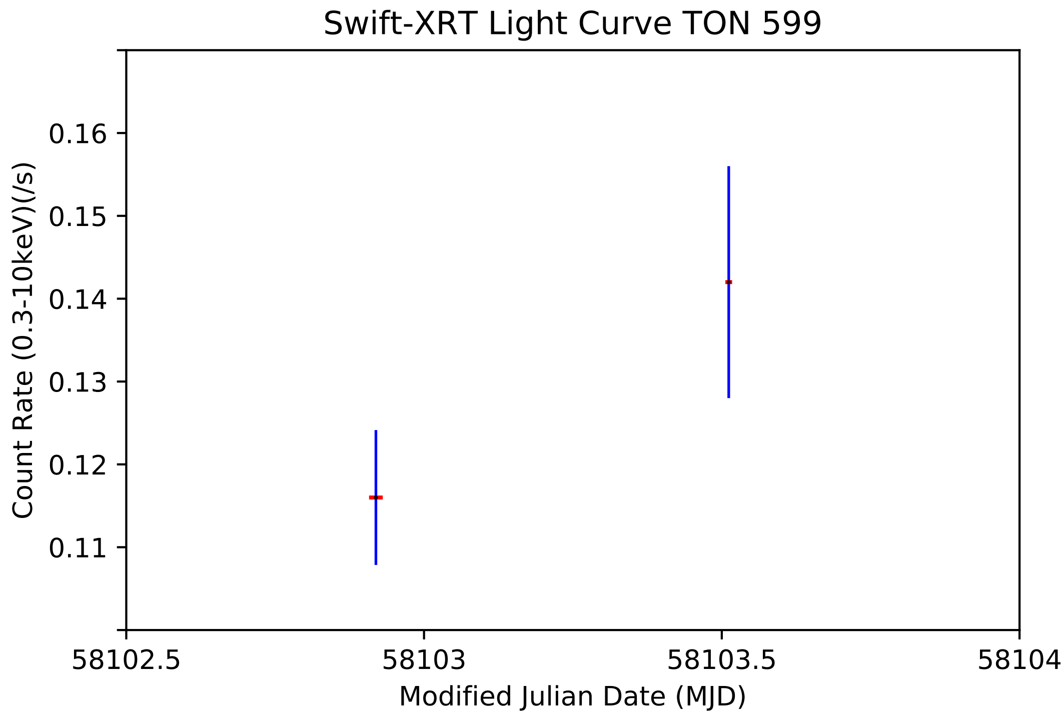

Figure 3.6: The light curve for MJD 58102 (December 15, 2017) and MJD 58103 (December 16, 2017) from Swift-XRT. The exact dates are MJD 58102.9192 and MJD 58103.5117 respectively. The red, horizontal error bars represent the duration of the observation and the observed count rate. The vertical blue lines are the uncertainty on the count rate.

3.2.2 The Fermi Gamma-Ray Space Telescope Data

The Large Area Telescope (LAT; Atwood et al., 2009) on the Fermi Gamma-Ray Space Telescope took observations of TON 599 during its flare. The data that Fermi observed are plotted in Figure 3.7 (Brill, 2018). Ideally, the VERITAS data would align with the Fermi data, but as seen in Figure 3.7, they do not. This could be in part because of the diminished reflectivity of the VERITAS mirrors due to aging. Another potential part of this discrepancy could be due to the fact that Fermi observed TON 599 over 48 hours while VERITAS observed TON 599 for only 2-3 hours. This means that the times that VERITAS and Fermi observed are different. It's possible that VERITAS observed at a time when the flare was less bright, while Fermi observed at times of higher brightness.

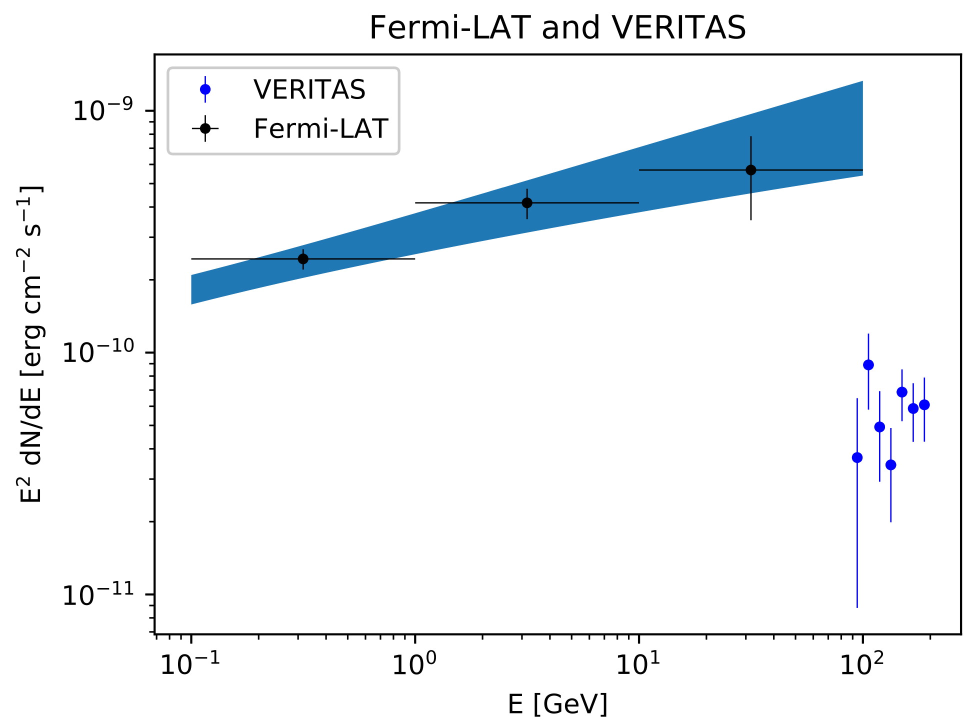

Figure 3.7: Fermi data plotted along with VERITAS data for the 2 day flare of TON 599. The black dots represent data from Fermi. The horizontal error bars represent the bin size, while the vertical error bars represent the error of $E^2\frac{dN}{dE}$. The blue shaded region is also Fermi data. This signifies the allowed region based on a power-law fit and combining the uncertainty on the normalization and the uncertainty on the spectral index. The blue points are the deabsorbed data obtained from VERITAS. The Fermi data were analyzed by Brill (2018).

3.2.3 VERITAS Spectra

Figure 3.8 is the spectrum that VEGAS creates after it has finished analyzing the data. The spectral index is -3.26 ± 0.63, which is the slope of the spectrum. The normalization energy, which is the energy at which the spectrum is centered, is 0.126. This value does not come from fitting the data, it is a value that is specified by the user. This spectrum has the same spectral points as the red spectrum in Figure 3.9. However, the spectrum in Figure 3.9 is refitted, shown by the red line. The flux normalization is the constant in the power law that the spectrum follows, represented as "Norm" in Figure 3.8.

Figure 3.9 shows the spectrum for the flare of TON 599. The red points show what we have observed and the blue points show what the spectrum looks like after we use the model of the EBL provided by Dominguez et al. (2011) to deabsorb the spectrum. This is what we expect to see; the deabsorbed spectrum having a higher flux than the observed spectrum, and it is not concave up. This means that the model for the EBL did not over-compensate for the absorption of gamma-rays. However, a softer spectrum for the deabsorbed VERITAS data than the Fermi data are also expected. In other words, we expect the absolute value of the spectral index to be greater for the deabsorbed spectrum than the Fermi spectrum. The spectral index for the deabsorbed VERITAS spectrum is -1.69$\pm$0.59 while the spectral index for the Fermi spectrum is -1.71$\pm$0.06. While the spectrum for the deabsorbed spectrum is not softer than that of the Fermi spectrum, the errors suggest that the two values are compatible.

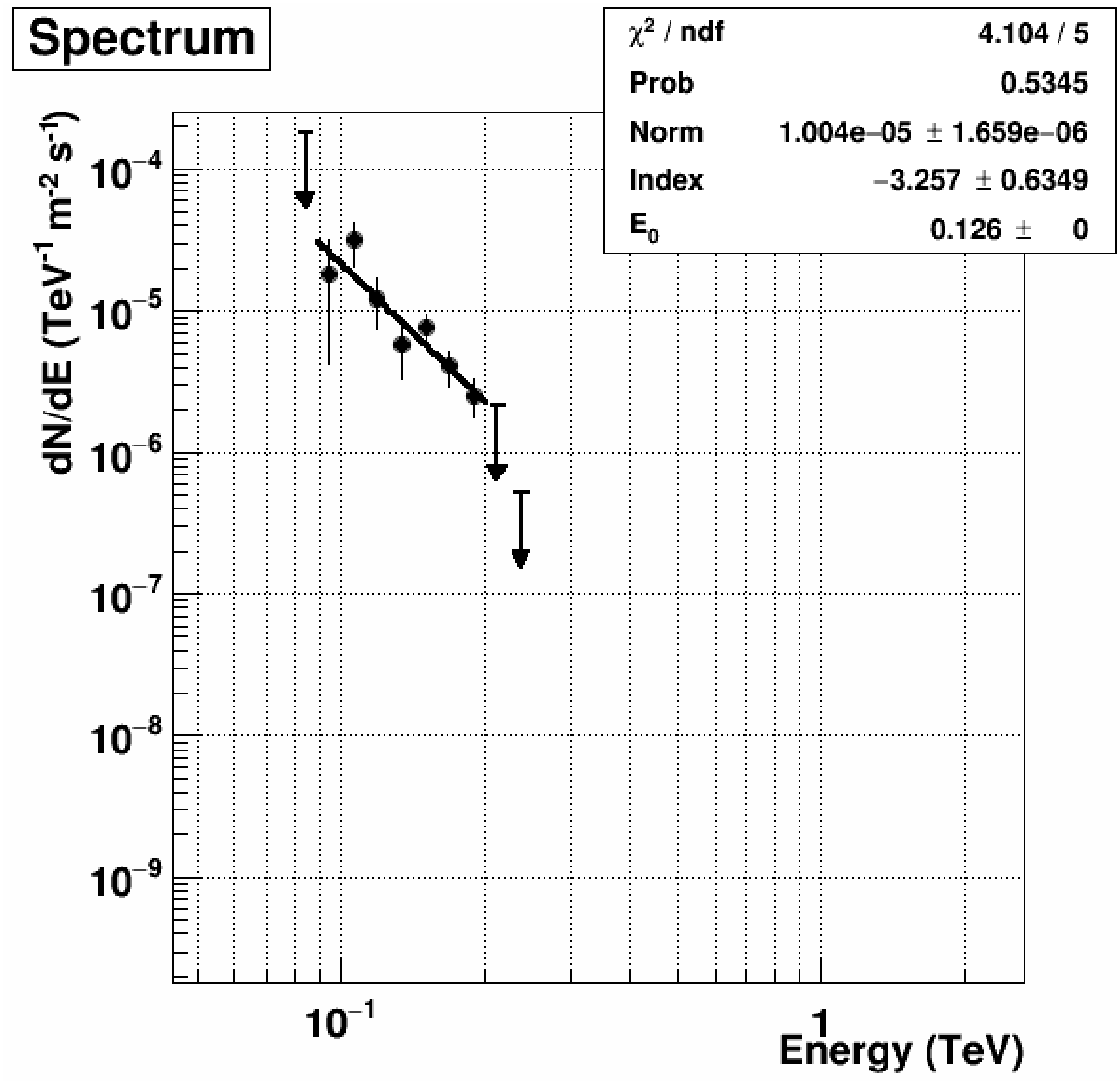

Figure 3.8: The spectrum created from the VEGAS analysis for TON 599 for MJD 58102 and 58103.

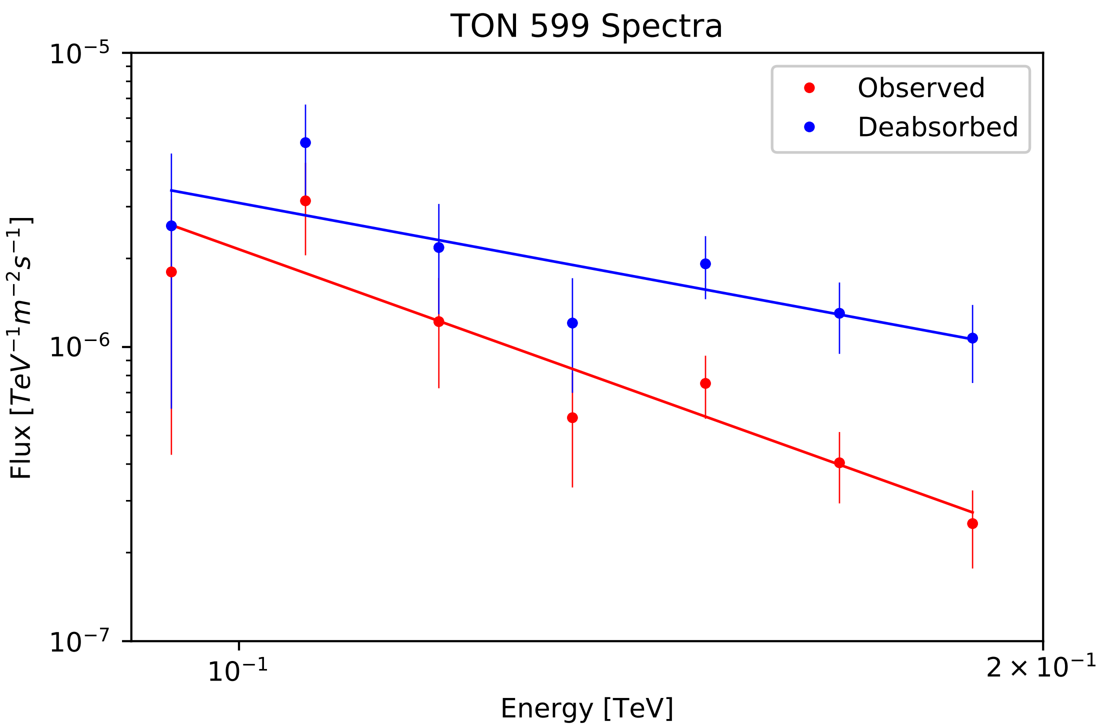

Figure 3.9: The observed and deabsorbed spectra for TON 599 for the combined data from MJD 58102 and MJD 58103. The red data show the observed spectrum and the blue data show the deabsorbed spectrum. The lines are the lines of best fit to their respective data.

4

Conclusion

TON 599 was chosen to test the Dominguez et al (2011) model of EBL due to the fact that its gamma rays are more heavily affected by the EBL because of its distance. TON 599 had a flare that lasted 2 days that was studied because the rest of the data were insignificant in comparison. The Dominguez et al (2011) model did not show anything unexpected, so the model was not disproven. Mrk 421 and Mrk 501 registered detections with significances of 297σ and 59σ respectively. PKS 1441+25 also registered a detection with a significance of 5.9σ. The flux values obtained from the VEGAS analysis are used in the creation of the light curves by Johnson (2018). PKS 1222+216 and 3C 279 did not register detections because they have a significance of -0.3σ and 0.6σ respectively. So, flux values are not obtained for these sources from the VEGAS analysis.

Appendix A

Runlists: Markarian 421

This appendix contains Mrk 421 runlists, whose formats are discussed in Section 2.3. This appendix has Tables A1, A2, A3, A4, and A5. These tables show the runlists for the different atmospheres that the observations were taken in and different configurations of telescopes. For example, Table A2 shows the runlist for the winter atmosphere and without telescope 2.

```
80283
80343
80586
80642 840/960 1080/1200 1380/1500
80685
80733
80956
81071 780/900
81335
81396
```

81397

81400

81401

81420

81439 2230/2240

81440 210/310

81518

81519

81970 120/360 758/859 960/1080

84014

84042 0/30

84107 660/720

84144

84289

84384 0/300

84399 0/480

84526

84698

84699

84700

84701

85059

85061

85069 0/130

85118

85289

85476

85477

85479

85482

85483 1560/1800

85582

85709

85743 0/120 540/780

85762

85813

85891

85983 0/45

88376

88391

88392

88393 600/900

88418

88419

88445 0/60

88446

88501 0/120 300/360

88502

88503

88504

88522

88523

88524

88525

88578

88591

88602 700/720

88701

88702

88703

88704

88705

88729

88730 300/429

88731

88732

88733

88734 1480/1490 1800/1980

88756

88757

88758

88759

88779

88780 150/270

88781 660/780

88782

88805 0/780

88806 525/1800

88807 510/810

88808

88809 720/1800

88810 1380/1800

88811 660/1200

88844

88848

88850 540/1800

88851 0/600 1080/1800

88865

88866

88867

88868

88870

88871 540/660

88872 1410/1500

88891 720/825

88892 1200/1800

88893

88896 300/660

88897 540/900

88898 0/1200

88920

88921

88922

88923

88929

88947

88953 0/840

88954

88977 0/40

88982 750/870 1080/1170

88893

88896 300/660

```
88897 540/900
88898 0/1200
88920
88922
88923
88929
88947
88953 0/840
88954
88977 0/40
88982 750/870 1080/1170
88983 720/810
89002
89005
89006
89047
89048
89260 172/293 540/1041 1304/1800
89530
89547
89586 0/360
```

Table A1: ATM21 (winter) runlist for Markarian 421 with all of the telescopes operational.

88544
88550
88551
88552
89509

Table A2: ATM21 (winter) runlist for Markarian 421 without telescope 2.

88473	
88474	
88476	
88477	1710/1800

Table A3: ATM21 (winter) runlist for Markarian 421 without telescope 3.

```
84354 0/960

84355 900/1800

84356
```

Table A4: ATM21 (winter) runlist for Markarian 421 without telescope 4.

```
86146 180/240

86206

86332 690/810
```

Table A5: ATM22 (summer) runlist for Markarian 421 with all telescopes operational.

Appendix B

Runlists: Markarian 501

As in appendix A, Tables B1, B2, B3, and B4 contain the runlists for Mrk 501.

```
81120

81121

81198

81199

81409

81410 170/185 520/540 870/885

81449 920/1162

81498 600/1200 1560/2401

81554

81638 1220/1240

81639

81836

81837

81921
```

81961 0/131 495/1001

81962 374/495 1446/1650

81971 0/120 270/330

81992

81993

81994

82022

82023

82991

83013

85837 540/720

85901

85973 150/390

85974

85975

86023

86076 780/790

86612 1820/1920

86676 1560/1800

86689 900/1800

87034

89605 90/1800

89768

89853

89909

89975

90071 1440/1800

90264

90360	1560/1800
90387	
90420	
90450	
90484	0/556
90485	

Table B1: ATM21 (winter) runlist for Markarian 501 with all of the telescopes operational.

82015	
82016	
82017	
86743	
86744	120/300
86746	180/300
89748	

Table B2: ATM21 (winter) runlist for Markarian 501 without telescope 1.

81556	
82990	

Table B3: ATM21 (winter) runlist for Markarian 501 without telescope 4.

86213	660/810
86320	210/360
86334	0/900
86358	0/615
86359	
86416	
86417	

Table B4: ATM22 (summer) runlist for Markarian 501 with all telescopes operational.

Appendix C

Runlists: PKS 1222+216

As in appendix A, Tables C1, C2, and C3 contain the runlists for PKS 1222+216.

80290

80565

80796

81031

81176

81370

81719

84500

84650

84976

85066

85790

85934

86123 690/797

Table C1: ATM21 (winter) runlist for PKS 1222+216 with all of the telescopes operational.

84266

Table C2: ATM21 (winter) runlist for PKS 1222+216 without telescope 2.

81953

Table C3: ATM21 (winter) runlist for PKS 1222+216 without telescope 3.

Appendix D

Runlists: PKS 1441+25

As in appendix A, Tables D1, D2, and D3 contain the runlists for PKS 1441+25.

```
77384

77385

77386

77387

77389

77390

77391

77392

77393

77403

77404

77405

77406  1300/1330

77408
```

77409

77410

77411 340/364

77412

77429

77430

77443 1650/1806

77444 480/1163

77453 0/600 1590/1802

77455

77467 0/180

77469

77470

77473

77474

77505

77631

77632

77633 90/245

77634

77635 180/300

77719

77720

77721

77857

78192

80595

81081

81217 0/45 310/330 870/900

81374

81618

81831

81998

84530

84733 540/600

84911

84912

85089 150/210

85369

85527

85878

85916 1140/1380

86014

89264 0/576

89267 630/840

89268 240/420

89269 1200/1800

89324

89580

89709

89926

90001

90069

90135

90209

90369

90480	0/720

Table D1: ATM21 (winter) runlist for PKS 1441+25 with all of the telescopes operational.

77978
89543
89544

Table D2: ATM21 (winter) runlist for PKS 1441+25 without telescope 2.

77472
77490
77491
77492

Table D3: ATM21 (winter) runlist for PKS 1441+25 without telescope 3.

Appendix E

Runlists: 3C 279

As in appendix A, Tables E1, E2, and E3 contain the runlists for 3C 279.

```
80597

80824

81035

81174 30/120

81373

81903

84652

84939

85085

85384 172/273 536/1173

85396

85578

85579 810/930

85602 1041/1284
```

85603

86127 0/151

88899 0/600

88900 510/690

88962 60/120

89901 0/600

Table E1: ATM21 (winter) runlist for 3C 279 with all of the telescopes operational.

84504 660/754

Table E2: ATM21 (winter) runlist for 3C 279 without telescope 4.

82236 0/60

90335 1560/1800

90336

```
90343

90344 1110/1410

90355 0/960

90366 0/300

90367

90383 0/180

90384

90400 870/930 1110/1170

90401

90431

90446

90447 1590/1650
```

Table E3: ATM22 (summer) runlist for 3C 279 with all of the telescopes operational.

Appendix F

Runlists: TON 599

As in appendix A, Tables F1 and F2, contain the runlists for TON 599.

```
88135 1810/1910

88356

88357

88378

88379

88380

88396 0/180

88397

88398 230/350 1060/1160

88420

88421

88422

88423

88447
```

88448	
88449	
88450	1060/1208

Table F1: ATM21 (winter) runlist for TON 599 with all of the telescopes operational.

88475

Table F2: ATM21 (winter) runlist for TON 599 without telescope 3.

Bibliography

Atwood, W. B. et al. (2009). The Large Area Telescope on the Fermi Gamma-Ray Space Telescope Mission. The Astrophysical Journal, 697(2), 1071. https://doi.org/10.1088/0004-637X/697/2/1071

Brill, A. 2018, private communication.

Dominguez, et al. (2011). Extragalactic background light inferred from AEGIS galaxy-SED-type fractions. Monthly Notices of the Royal Astronomical Society, 410(4), 2556. https://doi.org/10.1111/j.1365-2966.2010.17631.x

Evans, P.A. et al. (2007) An online repository of Swift/XRT light curves of γ-ray bursts. Astronomy & Astrophysics, 469(1), 379-385. https://doi.org/10.1111/j.1365-2966.2009.14913.x

Evans, P.A. et al. (2009). Methods and results of an automatic analysis of a complete sample of Swift-XRT observations of GRBs. Monthly Notices of the Royal Astronomical Society, 397(3), 1177-1201. https://doi.org/10.1111/j.1365-2966.2009.14913.x

Gehrels, N. et al. (2004). The Swift Gamma-Ray Burst Mission. The Astrophysical Journal, 611, 10051020. https://doi.org/10.1086%2F422091

Hanna, D. et al. (2009). An LED-based flasher system for VERITAS. Nuclear Instruments and Methods in Physics Research Section A 612(2), 278-287. https://doi.org/10.1016/j.nima.2009.10.107

Hauser, M. & Dwek, E. (2001). The Cosmic Infrared Background: Measurements and Implications. Annual Review of Astronomy and Astrophysics, 39. https://doi.org/10.1146/annurev.astro.39.1.249

Hewett, P. C., & Wild, V. (2010). Improved redshifts for SDSS quasar spectra: Improved SDSS redshifts. Monthly Notices of the Royal Astronomical Society, 405, 2302-2316. https://doi.org/10.1111/j.1365-2966.2010.16648.x

Holder, J. et al. (2006). The first VERITAS telescope. Astroparticle Physics, 25(6), 391-401. https://doi.org/10.1016/j.astropartphys.2006.04.002

Johnson, C. (2018). When Thermal Meets Non-Thermal: Investigating Gamma-Ray Emission From Very-High-Energy Blazars. Ph.D. Dissertation, University of California, Santa Cruz.

Mukherjee, R. (2017). ATel #11075: VERITAS Detection of VHE Emission from Ton 599. http://www.astronomerstelegram.org/?read=11075

Schneider, D. P. et al. (2010). The Sloan Digital Sky Survey Quasar Catalog V. Seventh Data Release. The Astronomical Journal, 139(6), 2360-2373. https://doi.org/10.1088/0004-6256/139/6/2360